Draft version May 25, 2026
Typeset using LaTeX default style in AASTeX631

Statistical and spectral analysis of carbon dioxide variations in terrestrial environment

Valentina V. Zharkova[1,2] and Irina Vasilieva[3]

[1] *Department of MPEE, Faculty of Engineering and Environment, University of Northumbria, Newcastle upon Tyne, NE1 8ST, UK*
[2] *ZVS Research Enterprise Ltd., London, EC1V 2NX, UK*
[3] *Department of Solar Physics, Main Astronomical Observatory, Kyiv, 03022, Ukraine*

ABSTRACT

We analyse the annual mean and annual growth rate measurements of the global CO_2 abundances taken from the NOAA General Monitoring Laboratory (GML). The annual CO_2 variations are shown to have the best polynomial fit by a parabola with concavity up that is contrary to the straight line assigned to a growth of CO_2 abundances produced by fossil fuel. The measured global CO_2 abundance variations were shown to correlate closely with variations of the Global Mean Sea Level (GMSL)(r=0.60), Oceanic Nina Index/El Nino Southern Oscillations (ONI/ENSO) (r=0.24) and global terrestrial temperature (r=0.82). The de-trended CO_2 abundance variations are found to have much stronger correlation with ONI/ENSO (r=0.79).

The spectral analysis with Morlet's wavelet of the variations of CO_2 abundances reveals the natural periods of 21.4, 9 and 3.7 years. The similar periods are derived for the variations of GMSL (21.4, and 8.5 years), ONI/ENSO index (21.4, 12 and 4.5 years) and the GLB terrestrial temperature (21.4, 8.36 and 3.75 years). The presence of a common period of 21.4 years indicates that all the datasets are affected by cyclic variations of the solar magnetic activity in a double solar cycle. The measured CO_2 oscillations with a period of 9 years combined with the correlation of the de-trended CO_2 abundances can be linked to the ONI/ENSO variations ranging within the periods of 4.5 and 12 years.

The cross-correlation analysis of global CO_2 abundance and terrestrial temperature variations reveals a time lag of about one year of the CO_2 abundance variations from the GLB temperature variations. Furthermore, the coherence wavelet analysis of the global CO_2 and GLB temperature datasets established a clear time lag of 1.2-1.8 years recorded for the CO_2 abundances with respect to the GLB temperature variations during most observing intervals. This indicates that global CO_2 variations follow the temperature variations and do not induce them.

Keywords: Data assimilation, Land/atmosphere interactions (1218, 1631, 1843, 4301), Statistical methods: Inferential (4318)

1. INTRODUCTION

The carbon dioxide (CO_2) abundance variations are often linked to the variations of terrestrial temperature and sea level variations.(Keeling et al. 1976) showing an steady increase of CO_2 abundances level which used since 1985 as the evidence for a recent concept promoting the man-made CO_2 increase in the industrial era. This increase of CO_2 assigned to the anthropogenic activity and use of fossil fuels was objected (Jaworowski et al. 1992; Trenberth & Fasullo 2009), who claimed that the errors in these revised values were of a similar magnitude to the apparent increase in the atmospheric CO_2 level imposed by the wrong assumptions such as: no liquid phase in polar ice; younger age of air than of ice due to free gas exchange between deep firn and the atmosphere; and no change in composition of air inclusions (Jaworowski et al. 1992).

Using two-dimensional regression analysis, Ahlbeck (2009) shown that the CO_2 increase rate could not be explained by the CO_2 emission because the fraction of the CO_2 emissions that remained in the atmosphere—or the airborne part—was shown to decrease significantly despite ongoing global warming. Ahlbeck (2009) suggested to explain this

effect by the increased diffusion or sink flow to the biosphere and the oceans due to the increased atmospheric partial pressure of carbon dioxide.

Soares (2010) compared the terrestrial temperature and CO_2 variations in the atmosphere is made for a large diversity of conditions reporting that CO_2 changes are closely related to temperature. It was shown that a weak dominance of temperature changes precedence, relative to CO_2 changes, indicate that the CO_2 increase in the atmosphere occurs mainly due to a temperature increase (Soares 2010). The author indicated that unlike CO_2 the water vapour in the atmosphere is rising in tune with temperature changes, even in a monthly scale (Soares 2010).

The partial pressure of CO_2 in seawater varies as the power of 12.5 of the absolute temperature (in Kelvin) of this water (Salby & Harde 2022) and, it is shown for the same quantity of carbon per kg of seawater, to be at 32°C about 3.2 times greater than at 5°C. The contrast in sea surface temperatures means that there is an oceanic carbon degassing zone and an absorption zone separated by several thousand kilometres.

The average CO_2 increase in the atmosphere, measured accurately by infrared spectrometry at Mauna Loa (NOAA, 2015), is 1.99 part per million (ppm) per year from 1995 to 2014 (Gervais 2016). The largest yearly increase observed in 1998, nearly 3 ppm, followed the largest El Niño warm fluctuation by 10 months. Other CO_2 increases above the mean such as 2.52 ppm in 2005, 2.42 ppm in 2010, 2.65 ppm in 2012 or 2.28 ppm in 2014, also follow by 9–11 months (Humlum et al. 2013). El Niño temperature fluctuations parameterised via the Multivariate ENSO (El Niño Southern Oscillation) index (MEI, 2014). ARIMA time-series modelling further supports the correlation between 12-month increments of MLO CO_2 and SST (Gervais 2016).

By contrast to these natural CO_2 variations, Veyres et al. (2024) reported no correlation between the de-trended 12-month CO_2 increments and fossil-fuel emissions. Veyres et al. (2024). suggested that only about 5.5% of the atmospheric CO_2 stock comes from fossil fuel emissions not yet absorbed by the vegetation or oceans, while 94.5% originates from natural outgassing of oceans and soils. This interpretation is supported by the δ^{13}C record at Mauna Loa Observatory (MLO). The 50% increase in vegetation productivity since 1900 can be attributed to higher atmospheric CO_2 concentrations and a longer growing season. Therefore, decarbonisation policies may affect only 5.5% of atmospheric CO_2.

The studies by different authors (see, for example, Salby et al. 2012; Easterbrook 2016; Roy 2018, and references therein) addressed the role of natural factors (the sun and volcanic eruptions) comparing to that from CO_2 led linear anthropogenic contributions. (Roy 2018) identifies that dominance of Central Pacific (CP) Ocean Nino Index (ONI) or El Nino Southern Oscillation ENSO) and associated water vapour feedback during that period play an important role in formation of CO_2 variations that confirms the suggestions by Salby et al. (2012).

In addition, Ato (2024) finds the ocean temperatures, not human-made carbon dioxide emissions, are the primary drivers of the atmospheric CO_2 changes. confirmed by another research (Ahlbeck 2009; Salby & Harde 2022). Furthermore, Koutsoyiannis et al. (2023) have shown that the causal relationship between an increase of the terrestrial temperature and a growth of the CO_2 abundances clearly indicates that the CO_2 presence must be a consequence of the terrestrial temperature growth and its reason as assumed by the modern temperature models (IPCC 2025). This leaves the question still open about the major features in the variations of CO_2 abundances and their established links with the variations of other terrestrial entities.

The aim of the current study is to investigate the available observational features for CO_2 abundances and to carry out statistical and spectral analysis of the relevant datasets, in order to recover any links in these variations with the other key key parameters of terrestrial environment, such as: the terrestrial temperature, the mean ocean temperature and sea level and the ONI/ENSO index, which is tele-connected with the other parts of the Globe.

2. DESCRIPTION OF THE TERRESTRIAL ENVIRONMENT DATA

2.1. *Observations of carbon dioxide variations*

For the variations of carbon dioxide let us utilise the data provided by the NOAA's Global Monitoring Laboratory (GML), which measures the abundances of carbon dioxide and other greenhouse gasses in the air using the global network of the data collection points (Conway et al. 1994). The data are provided in the mole's part, measured in particles per million (ppm), of a dry air, which defines a number of carbon dioxide molecules in the air after removing the contribution of the water vapour.

The carbon dioxide data for MLO, Samoa and the global one, e.g. the data averaged from all the stations using Monte Carlo approach as described by Lan et al. (2026) We use two CO_2 datasets: 1) globally averaged marine surface CO_2 annual mean data: https://gml.noaa.gov/ccgg/trends/gl_data.html; https://gml.noaa.gov/webdata/ccgg/trends/co2/

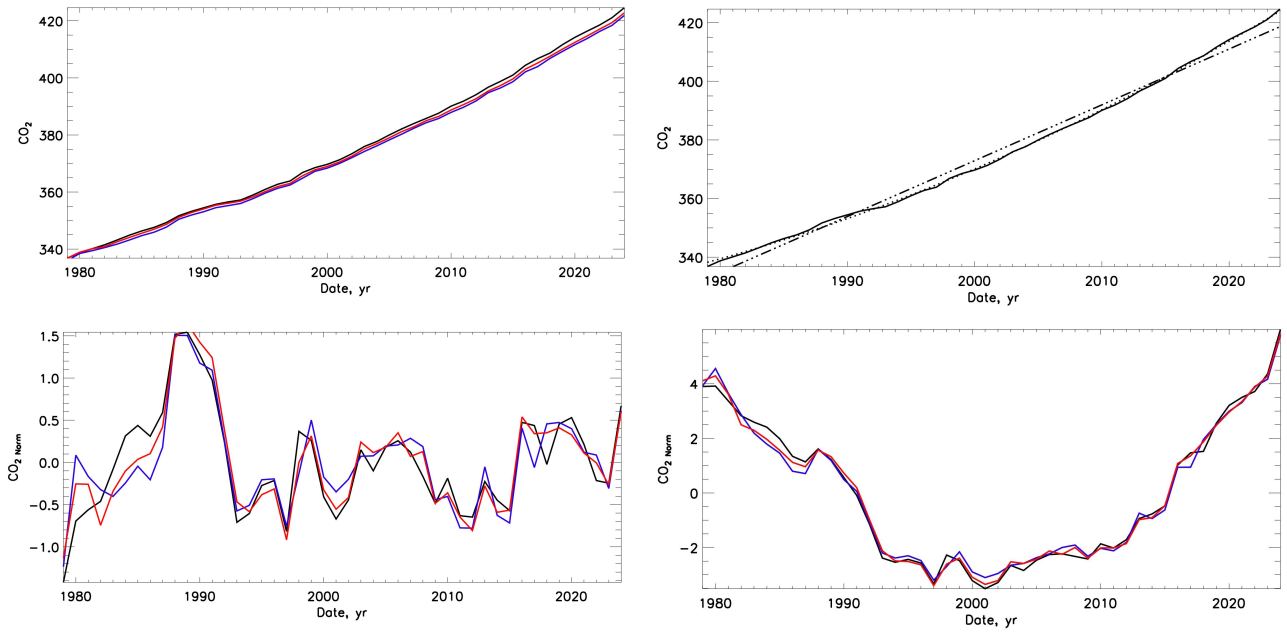

Figure 1. Top plot: the annual variations of CO_2 abundances observed in Samoa (blue curve), MLO (black curve and global (red curve) (left) and approximation of global CO_2 abundances by a linear approximation. Bottom plot: the deviations of CO_2 abundances from their parabolic (left) and linear (right) approximations.

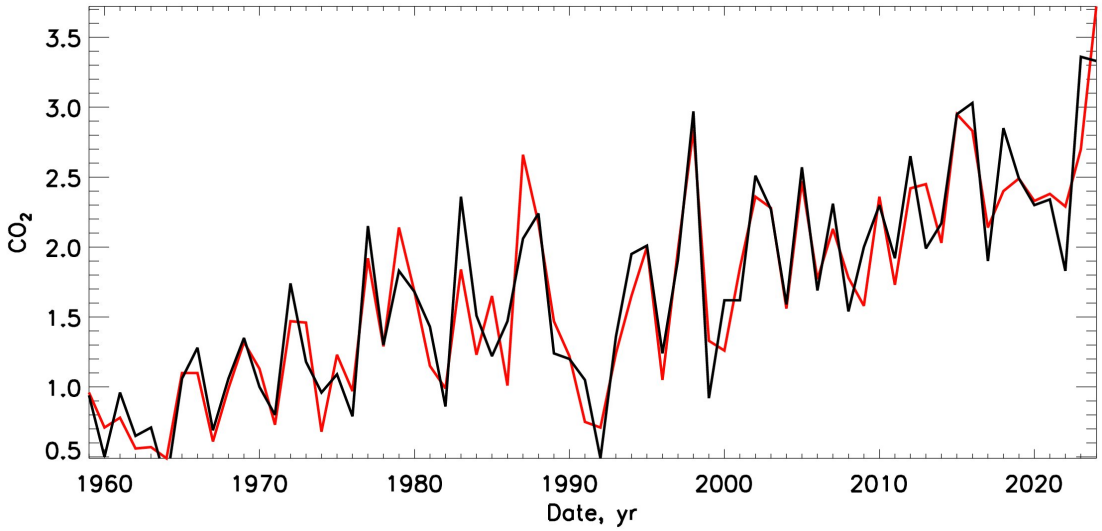

Figure 2. The variations of CO_2 abundances (growth rate) measured by the MLO (black curve) and derived from all the stations, as global CO_2 variations (red curve).

co2_annmean_gl.txt and 2) globally averaged marine surface annual mean CO_2 growth rates: https://gml.noaa.gov/ccgg/trends/data.html; https://gml.noaa.gov/webdata/ccgg/trends/co2/co2_gr_gl.txt.

The annual mean (averaged0 CO_2 data is shown in Fig.1 and the growth rate CO_2 data variations are presented in Fig.2.

The key points of CO_2 measurements include the following locations: Barrow, Alaska (BA); Mauna Loa Observatory (MLO), Hawaii; American Samoa (Samoa) and Southern pole (SP), Antarctica. Since 1973 the GML secures the uninterrupted measurements of the carbon dioxide abundances (Thoning et al. 1989) that allows one to derive a high level of details in the seasonal, short-term and long-term variations of these carbon dioxide abundances. The series

of the MLO observations in the northern subtropics is obtained at the height of 3400 m above sea level provide the longest observations of carbon dioxide abundances started in March 1958 by C.David Keeling (Keeling et al. 1976). Because of its height of 3400 m above the sea level, the MLO data have some understandable systematic differences from the other data measured close to the surface at the sea level. annual variations of CO_2 abundances measured by Samoa, MLO and global data shown in Fig.**??** reveal that global variations reflect very closely the CO_2 variations measured by Samoa or MLO sites. The polynomial approximation of the global CO_2 variations (solid curve) was conducted by a linear (dash-dotted curve) (Fig.1, top right plot) and parabolic approaches (not shown as it fits closely the observed curve shown in Fig.1, top left plot). The deviations of the measured global CO_2 curve from the polynomial approximations are shown in Fig.1, bottom plots for parabolic (left) and linear (right) fits.

It can be observed that the linear polynomial fit reveals a systematic deviation of the linear curve from the observed one between 1990 and 2015 (Fig.1, bottom right plot) clearly seen in a comparison between solid (observed) and dash-dotted curves (linear fit). While the parabolic polynomial fit shows a normal deviation of the differences between real and parabolic curves reflecting a good approximation. These differences in the deviations of the real CO_2 annual curve and polynomial fits indicate that the measured global CO_2 variations are best described as a positive parabolic function indicating a concavity up of the measured curve (the parabola opens upward) and not by a linear curve assigned by IPCC to the increase of CO_2 from a usage of fossil fuel. This means that the measurements of the total (global) CO_2 variations, which by default should be present in the measured data, do not reveal any noticeable similarity to the linear CO_2 abundances produced by the fossil fuel usage.

The examples of real (not annually averaged) trends in the CO_2 abundance variations measured by MLO and global data are presented in Fig.2. This comparison show pretty close correspondence of both the datasets while revealing noticeable temporal fluctuations of the real CO_2 abundance data. These measured CO_2 variations can be explored for comparison with the other terrestrial data as discussed in section 2.2 and used for the wavelet spectral analysis described in section 4.

2.2. *Observations of temperature, sea level and Ocean Nina Index (ONI)*

2.2.1. *The terrestrial temperature variations*

In this research we consider the two series of terrestrial temperature measurements, which have a global coverage of the terrestrial regions not affected by any local phenomena, like El Nino/La NIna events in the Pacific ocean area. The first set is developed by the British Meteorological Center in Hadley and the department of Climate Research of the East Anglia University https://www.metoffice.gov.uk/hadobs/hadcrut5/ (Morice et al. 2021), accessed on 12/06/2023. This series starts from 1850 and named as HADCRUT5 for the future reference. The second set is the series of the surface temperature (GISSTEMP) produced by the NASA Goddard Institute of Space Science (GISS) https://data.giss.nasa.gov/gistemp/tabledata_v4/GLB.Ts+dSST.txt accessed 12/06/2023 Lenssen et al. (2019), so it will be called GLB hereafter.

The both sets are shown in Fig.3 in the top plot for the HADCRUT5 set (red curve) and GLB set (black curve) and in the bottom plot there is a difference of these two datasets is presented. It can be seen that the two temperature datasets are rather close besides in the interval of 1880-1910 when GLB set has systematically higher magnitudes. The difference between these two series seems to be not so large as shown in Fig.3. Although it leads to some noticeable discrepancies revealed during the analysis of the periodic part of the series discussed below. In order to exclude the effects of limited lengths of the series, for a comparison with CO_2 variations we will use the GLB data. The GLB temperature variations will be compared with the variations of CO_2 abundances in section 4.2.3.

2.2.2. *The sea level variations*

The series of temporal variations of the Global Mean Sea Level (GMSL) during 1880-2014 (named as GMSL(2015)) was obtained from the Centre for Protection of the Environment of the USA and SCIRO (Centre for Scientific and Industrial Research Organisation) (http://www.cmar.csiro.au/sealevel/sl_data_cmar.html accessed on 29/07/2023 (Church & White 2011).

The GLB temperature (black curve) and its approximation by the 4th degree polynomial (red curve) is shown in Fig.4 (top left plot) with real GMSL measurements (black line) and the averaged one by the 4th-order polynomial (red line) are shown in Fig.4 (top right plot). In Fig.4, bottom left plot there are the de-trended GMSL sea level variations (black curve) calculated by subtracting from the data defined by the the averaged data shown in Fig. 4, top right plot, versus the GLB temperature (blue plot) and the summary curve of the solar magnetic activity (red curve) (Zharkova et al. 2015).

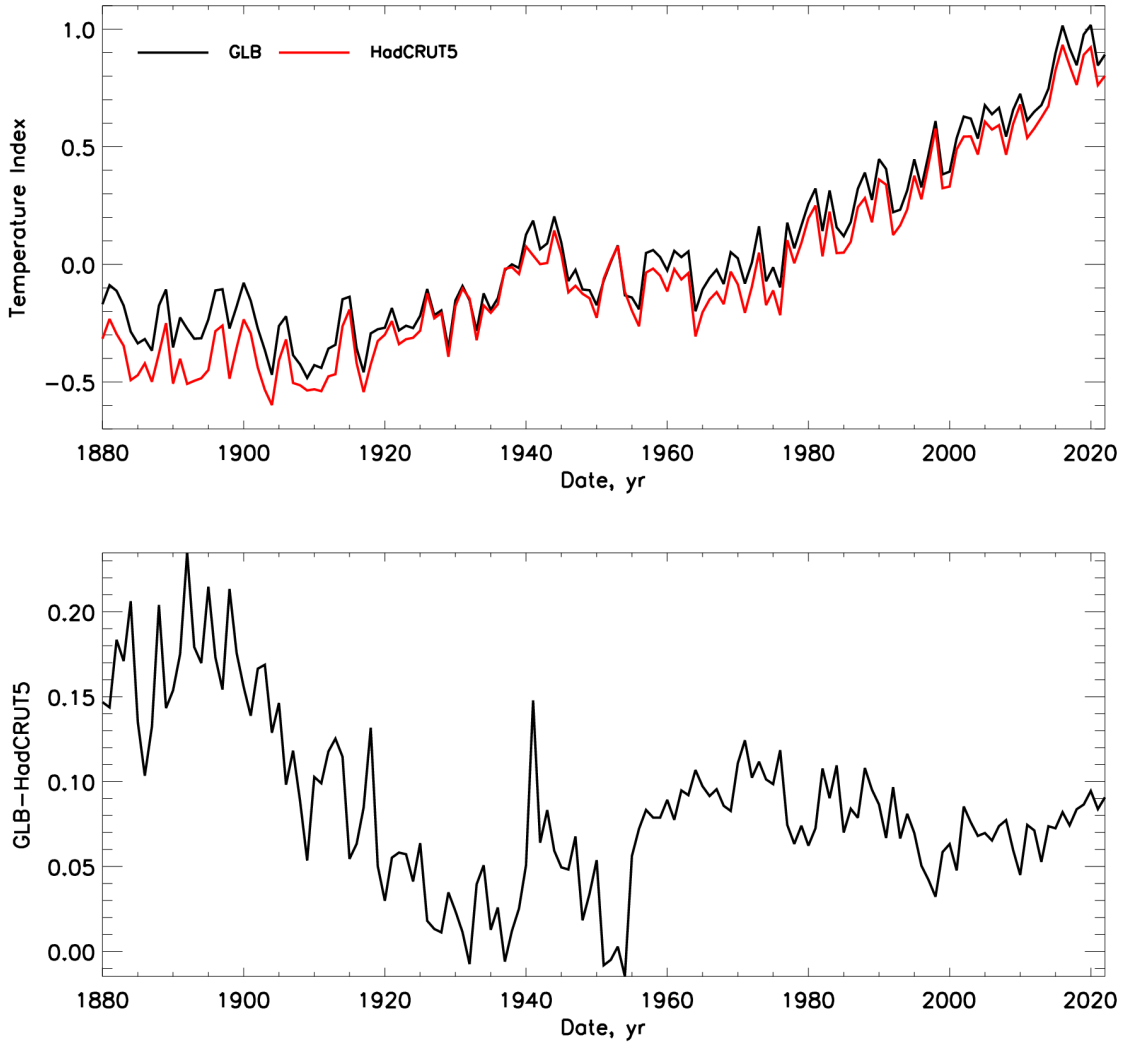

Figure 3. Top plot: the series of terrestrial temperature variations HADCRUT5 (red curve) and GLB (black curve). Bottom plot: the difference between GLB and HadCRUT5 data..

In Fig.4, bottom right plot there is comparison of the GMSL data extended to 2019 (named GMSL (2019)) with the GMSL data measured by 2014 (named GMSL (2015)) which was used in our previous research (Zharkova & Vasilieva 2023). The data for 2019 were corrected by the increased normalisation by 128 mm combined with strong variations of the measurements after 1990. To avoid these fluctuations, In the current paper we mainly used the first (uncorrected) dataset of GMSL (2015) as there were no explanation provided by the site for the corrections in the set GMSL (2019).

It can be observed that the sea level was increasing from 1870 until 2004 with an averaged speed of growth of 1.7±0.3 mm/year (Church & White 2006), or of 3.1 ± 0,7 mm/y (Cazenave & Nerem (2004); Leuliette et al. (2004). Although during the period of 1971-2018 and 3.7 (3,2-4.2) during the period of 2006-2018 he average growth speed of 2.3 rangied from 1.6 to 3.1) mm/y. Fox-Kemper et al. (2021).

This increase of the GMSL sea level show, in average, a close similarity to the temporal variations of the GLB temperature curve reported in the previous studies (Rahmstorf 2007; Nerem et al. 2018; Storch et al. 2008; Grinsted et al. 2010; Vermeer & Rahmstorf 2009; Sannino et al. 2022; Zharkova & Vasilieva 2023). Furthermore, the de-trended fluctuations of the GMSL sea level (blue curve) shown in Fig.4, bottom left plot, follow closely the GLB temperature variations (black curve). In addition, these GMSL and GLB variations reveal some links with the solar magnetic activity with a period of 21.4 years (red curve) as it was noted earlier Zharkova & Vasilieva (2023). The GMSL variations will be compared with the variations of CO_2 abundances in section 4.2.1.

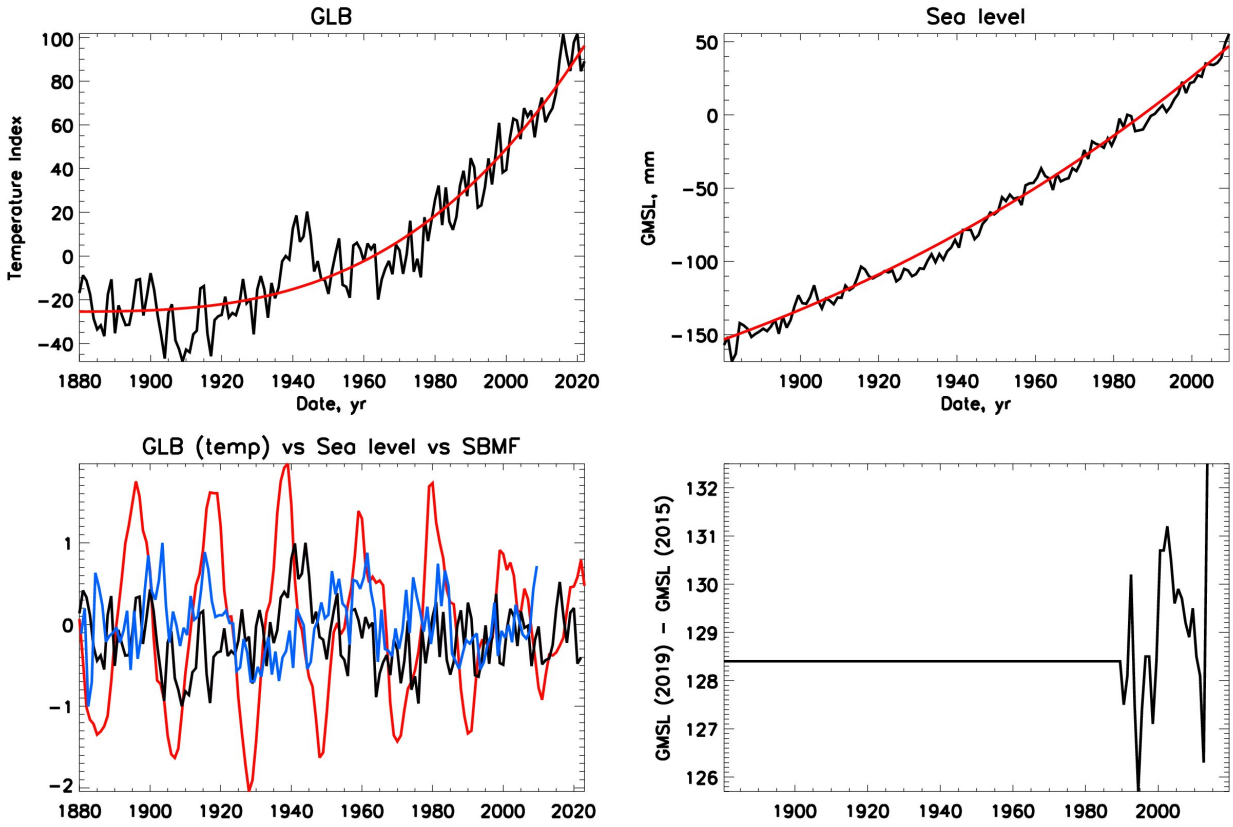

Figure 4. Top plot left: the variation of global GLB temperature (black curve) and approximation by a polynomial of 4th degree (red curve), Top plot right: the global mean sea level (GMSL) variations for 1870-2014 (black curve) and averaged curve presented by a polynomial of the 4th degree (red curve). Bottom left plot: comparison of the GLB temperature variations (black curve) with the de-trended sea level variations (blue curve) calculated by subtracting the averaged sea level from the real sea level curve. The red curve represents the summary curve of solar background magnetic field defining the magnetic solar cycle of 21.4 years (Zharkova et al. 2015). Bottom right plot: a comparison of the two temporal versions of GMSL releases in 2015 and 2019 with renormalisation by 128 mm in 2019 and introduction of some unrecognised measurements from 1990 onwards.

2.2.3. *The Oceanic Nina Index, or El Nina Southern Oscillations (ONI/ENSO)*

The Oceanic Nina Index (ONI,) which also called as El Nina Southern Oscillation (ENSO), e.g. the ONI 3.4 index, is available since 1854 Kaplan et al. (1998). ONI index follows the three months measurements of an average temperature of the sea surface in the East-Central tropical part of the Pacific ocean nearby the international line of the date change above the averaged one over 30 years. The Oceanic Niño Index (ONI) is taken from the site https://www.climate.gov/news-features/understanding-climate/climate-variability-oceanic-nino-index.

The temporal variations of the ONI/ENSO index from 1950 till present is shown in Fig.5, bottom plot, where the red colour shows the excesses above the averaged ENSO index and the blue colour shows the reductions below the averaged index. Fig.5 shows the temporal variations of the Global Land-Ocean Temperature (GLB) Index (black curve) (Lenssen et al. 2019) versus variations of ONI/ENSO Index (multi-coloured curve).

From a comparison of the curves tone can observe that there is a strong visible link between the ONI/ENSO index and the increase of the global land-ocean t(GLB) temperature. The scatter plot of correlation of the ENSO and GLB temperature curves is shown in Fig.6 reveals a very strong correlation covering the majority of the data within 95% confidence interval. The Pearson and Spearman correlation coefficients calculated in assumption of normal and multivariate data distribution are equal to 0.887 and 0.863, respectively, with a significance level of $P < 0.001$.

Previously, it was shown by Zharkova & Vasilieva (2024a) that the correlation coefficient between the averaged sunspot index and the ONI/ENSO index is close to zero (r=0.01), and it is slightly better but still low (r=0.10) for the correlation of the ENSO index with the solar magnetic cycle of 21.4 years, e.g. the summary curve of SBMF (Zharkova

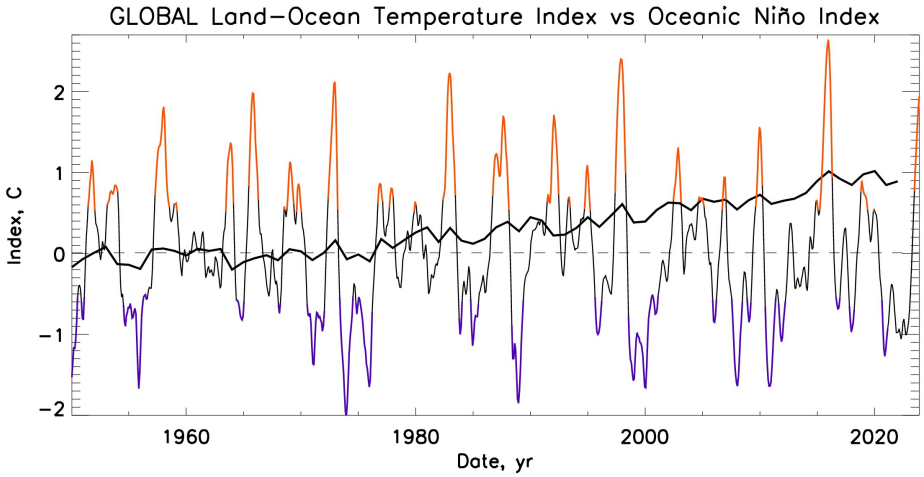

Figure 5. Temporal variations of the combined land-surface air and sea-surface temperature, GLOT (black curve) and of the Oceanic Nina Index (ONI), or El Nina Southern Oscillation (ENSO) index (multi-coloured curve). The red colour shows the excesses (hot periods) above the averaged ONI/ENSO index and purple colour shows the reductions (cold periods) below the averaged ONI/ENSO index.

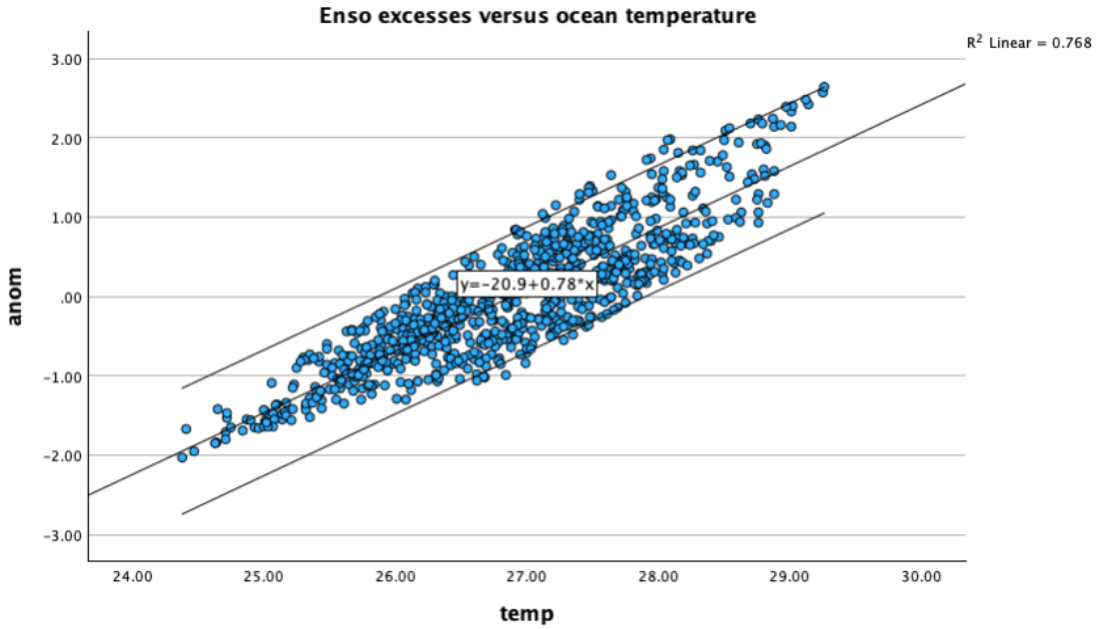

Figure 6. Scatter plots of the correlation of the ONI/ENSO index variations and the global land-ocean temperature (r=0.89) approximated by linear fit (central line, top plot). The outer thin lines define the 95% confidence intervals, the χ^2 coefficients is equal to 0.768 as presented in the top right corner.

et al. 2015). The ONI/ENSO was shown to have strong effects by moon gravitation induced by the oscillations of the lunar perigee, revolution of Jupiter and orbital motion of Sun imposed by the gravitation of large planets (Zharkova & Vasilieva 2024b), which provides a noticeable link of the ONI/ENSO index with the frequency of under-water volcanic eruptions, which, in turn, are affected by the solar magnetic cycle of 21.4 years (Vasilieva & Zharkova 2023).

3. SPECTRAL ANALYSIS OF TIME SERIES WITH A WAVELET TRANSFORM

In order to understand the nature of ongoing variations of different measurements of the terrestrial environment , such as variations of land-sea temperature, sea level, ONI/ENSO index and carbon dioxide abundances, let us explore their spectral properties using a wavelet analysis.

3.1. *General description of the wavelet transform analysis*

The series of the time-dependent data considered in the terrestrial environment are generated by complex processes, which are not fully known or understood. The most essential interests in such the systems are the ways to anticipate their appearances in the future. Most traditional mathematical methods investigating periodicities in a frequency domain, such as Fourier analysis, implicitly assume that the processes which form the temporal series are stationary in time that is not always the case.

While the wavelet transform allows to expand a temporal series into the frequency-time domain that allows to detect local patterns of a temporal series under investigation. Wavelet transform is a very useful instrument for the analysis of localised interruptive oscillations in the temporal series. The wavelet analysis is most beneficial for investigation of coupled time series which are somehow linked by natural processes forming them but not clearly known to the investigators. Even more beneficial for detecting these links is a cross-wavelet transform deriving the correlation and its relative phase in the time-frequency domain.

Continuous wavelet transform (CWT) of signals is the spectral analysis method providing a two-dimensional scan of the analysed signal (time and frequency, or period), in which the coordinates of the time and frequency are independent variables (Torrence & Compo 1998) as defined below

$$W_x(u,s) = \int_{\infty}^{\infty} x(t)\frac{1}{\sqrt{s}}\Psi\left(\frac{t-u}{s}\right)dt, \tag{1}$$

where u is temporal position, s is scale (inverse to frequency), and $\Psi = \Psi^M$ is Morlet wavelet defined as follows:

$$\Psi^M(t) = (\pi^{-\frac{1}{4}})e^{i\omega_0 t}\cdot e^{-\frac{t^2}{2}}, \tag{2}$$

where $\omega_0 = 6$ for most geophysical applications (Vacha et al, 2012).

This representation allows one to explore the properties of the signal simultaneously in time and frequency domains. This makes the wavelet analysis an excellent tool for examining the series with time-varying frequency characteristics (Torrence & Compo 1998). By considering the time series in the frequency-time space it is possible to derive dominant periods and their variations in time. The mother wavelet was selected as the Morlet wavelet (the real part of it is damped function of cosine), because with this choice one can obtain a high frequency resolution, which is important for our task.

The power of the wavelet spectra is shown in plots with wavelets by a colour bar plotted next to the wavelet spectrum. The Cone of Influence (COI) marked in the wavelet spectrum by the black dashed line, defines the parts of the spectrum with the essential border effects in the starting and finishing parts of the time series, because of a limited statistical data (boarder effects). Consequently, the results outside the COI are excluded from the further investigation, particularly, in the calculations of the global wavelet spectrum shown by the black curves on the right hand side from the wavelet spectra where we present by the solid black lines the global wavelet spectra integrated over time. The black dashed lines in the global wavelet plots presents 95% confidence interval for the global wavelet spectrum.

3.2. *Cross-wavelet transform and wavelet coherence*

One of the main advantages of using the Morley wavelet transform is the function of a wavelet coherence. Wavelet coherence is built on the continuous wavelet transform (CWT), which projects a time series x(t) onto a set of time- and scale-localised basis functions (wavelets). Usually, the coherence function is used in practical application for establishing a reliable link of the processes in the frequency domain by allowing to establish a correlation of two time series in the domain of time-frequency.

Assuming there are two time series x(t) and y(t), their cross-wavelet transform can be defined as:

$$W_{xy}(u,s) = W_x(u.s)W_y^*(u,s). \tag{3}$$

from which the squared wavelet coherence is defined as follows:

$$R^2(u,s) = \frac{|S(s^{-1}W_{xv}(u,s))|^2}{|S(s^{-1}W_x(u,s))|^2|S(s^{-1}|W_y(u,s))|^2}, \tag{4}$$

where S is a smoothing operator in both time and scale that prevents from overfitting to a transient noise. The coherent function R^2 is ranging from 0 (no local correlation) to 1 (perfect local correlation).

Phase shift information is available through the argument of the smoothed cross-spectrum using its imaginary $\Im$ and real $\Re$ parts as follows:

$$\Delta\phi_{xy}(u,s) = \tan^{-1}\left(\frac{\Im[S(s^{-1}W_{xy}(u,s))]}{\Re[S(s^{-1}W_{xy}(u,s))]}\right), \tag{5}$$

which quantifies in-phase or anti-phase behaviour and a possible lead lag relationship.

Then the time lag $\Delta t(x,t)$ is calculated via the phase shift $\Delta\phi_{xy}$ as described below:

$$\Delta t(x,t) = \frac{\Delta\phi_{xy}(s,t)}{2\pi \cdot f(s)}, \tag{6}$$

where $f(s)$ is a frequency corresponding to the scale s, $\Delta\phi_{xy}$ is the phase angle in radians.

When the two series are in phase, the arrows are inclined to the right, e.g. the phase shift is positive, it means the series move in the same direction. While when the arrows are inclined to the left, or phase shift is negative, the series are in anti-phase meaning they move in the opposite directions (Grinsted et al. 2004). The angles of inclination of the arrows on the wavelet coherence plot would indicate the phase relationship between the series, either one moving forward or lagging another. Hence, the angle of the arrow inclination indicate the phase angle shift $\Delta\phi$, which can be linked to the time lag Δ_t as per Eq. (6) above.

4. RESULTS OF SPECTRAL ANALYSIS OF CARBON DIOXIDE IN COMPARISON WITH OTHER TERRESTRIAL DATASETS

4.1. *Spectral variations of total CO_2 abundances by different stations*

The global spectral characteristics of CO_2 variations are found to be rather similar with that in MLO revealing the well defined (above 95% confidence level) periods of oscillations of 9 and 21.4 years and the period of 3.79 years occurring just within the 95% confidence level as it shown in Fig.7 in the global wavelet spectra depicted on the right side of the wavelet images.

The period of 21.4 years derived in the wavelet spectra for global and MLO variations of CO_2 is clearly linked to the variations of the solar activity expressed through the summary curve of the two eigen vectors of the solar background magnetic field (Zharkova et al. 2015), which has a double period of the solar activity cycle of 10.7 years defined by the sunspot numbers (Zharkova et al. 2023b). Evidently, the maximum CO_2 is produced during the solar cycles with a dominant southern magnetic polarity occurring in the even cycles which producing the maximal geomagnetic effects on the terrestrial magnetosphere and atmosphere.

The oscillation periods of 9 and 3.79 years have less certain links with the solar activity as such, but might be linked to the combined effects of some other factors of the terrestrial environment like global mean sea level (GMSL) and El Nino Southern Oscillations (ENSO), which, in turn, are found to be affected by gravitation of Jupiter on the Sun and Earth and of Moon via the small- scale oscillations of the lunar perigee (Zharkova & Vasilieva 2024b). These points will be discussed in sections below.

4.2. *Spectral analysis of carbon dioxide in comparison with other terrestrial datasets*

4.2.1. *Comparison of CO_2 and sea level variations*

Let us first compare the datasets of the MLO CO_2 abundances with the variations of global sea level taken from the GMSL dataset as shown in Fig.8, It can be noted that there is a general trend of increasing in time of CO_2 and GMLS sea level (Fig.8, left plot), although the increase of CO_2 abundance looks faster than an increase of the sea level.

This is reflected in the correlation coefficient r=0.60 between these two datasets as demonstrated by the scatter plot in Fig.8, right plot. The scatter plot also shows a better fit by quadratic curve indicating a trend of mild saturation of the sea level effect in the production of CO_2. This indicates that despite the ocean-air exchange is rather intense and important for producing CO_2 presence in the air there are some other mechanisms affecting the CO_2 abundances, which grow faster than the increase of the sea level and temperature.

In order to gain more information about the changes let us run a spectral wavelet analysis of the GMSL datasets (2015 and 2019) shown in Fig.9 and compare these with the wavelet spectrum obtained for the global and MLO CO_2 abundances shown in Fig.7. It can be observed from the global wavelet spectra in the right bottom plots in both

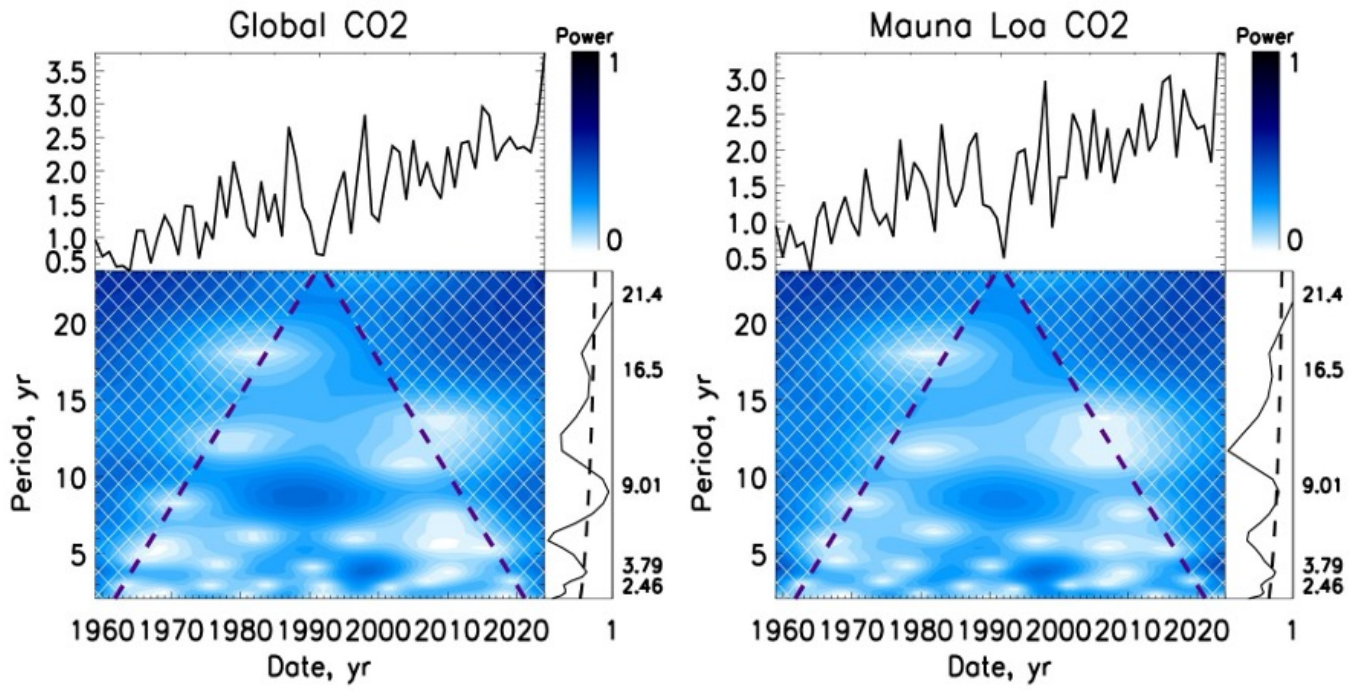

Figure 7. The wavelet analysis of the variations of the global (left) and MLO (right) CO_2 abundances. The CO_2 global and MLO variations are plotted in the top left sides of each image with their wavelet spectra shown in the bottom left sides of each image with the black dashed lines showing the Cone of Influence (COI). The wavelet spectral powers are marked by the colour bars in each image (the top right plots) and the global wavelet spectra (black solid line) integrated over times are shown in the bottom right plots with the black dashed lines indicating the 95% confidence intervals of the detected spectral features.

CO_2 datasets (global and MLO) that there is a dominant (well above 95% confidence level) 21.4-years period of the variations for CO_2 datasets, as it was shown for CO_2 in section 4.1 and for the sea level GMSL with a period on 19.6 years shown in the wavelet spectra of the both GMSL dataset shown in Fig. 9.

The similar period of 21.4 years correspond exactly to the period of solar magnetic activity variations shown in the summary curve of the eigen vectors of solar background magnetic field (Zharkova et al. 2015, 2023b). This double magnetic activity period of 21.4 years in CO_2 abundance variations indicates the undeniable natural effect of the Sun and solar radiation on the generation of carbon dioxide in the terrestrial atmosphere. This means any other (like anthropogenic) contributions to the CO_2 abundances are significantly lower than the natural ones that confirms the previous similar conclusions claiming only 5.5% contribution by fossil fuels (Salby & Harde 2022; Veyres et al. 2024).

In addition, there is the other period of CO_2 variations of about 9 years clearly observed above the 95% confidence level, which can be linked to the similar period of 8.26 years in GMSL spectrum marked just at the border of this confidence level. This period of 9 years indicates to a possible link between the CO_2 variations with sea level and temperature variations as well as with the other phenomenon like ONI/ENSO index, which is discussed in the next section.

4.2.2. *Variations of the total CO_2 abundances versus ONI/ENSO variations*

Comparison of the temporal variations of CO_2 abundances and ONI/ENSO index is shown in Fig.10 (left plot) and the scatter plot of their correlation in Fig.10 (right plot). It demonstrates a pretty moderate correlation of 24% indicating the ONI/ENSO index as such. does not strongly affect the global CO_2 abundance appearances.

Although, a different story appears from a comparison of a de-trended plot of the global CO_2 abundances and ONI/ENSO variations shown in Fig.11, which show much stronger (79%) correlation. This indicates that CO_2 deviations from the averaged CO_2 abundances are significantly affected by the variations of ONI/ENSO index. Combined with the significant (60%) correlation of the global CO_2 with the sea level GMSL dataset this correlation indicates a significant role of exchange of CO_2 between the ocean and air based on Henry's law (Henry 1803).

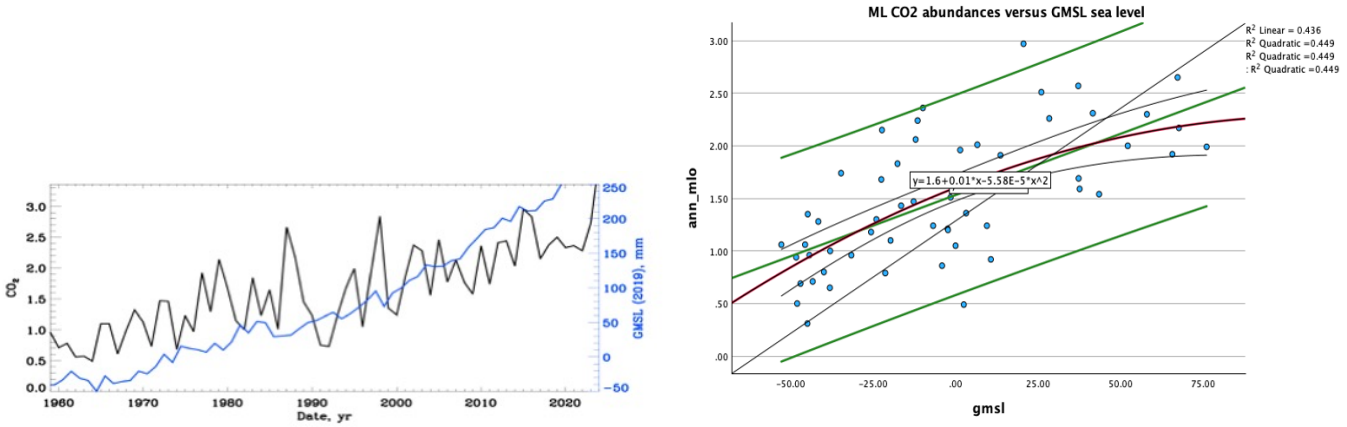

Figure 8. Left plot: comparison of variations of the MLO CO_2 abundances (black curve) versus the Global Mean Sea Level (GMSL) variations (blue curve). Right plot: the scatter plot of the correlation (r=0.60) of the MLO CO_2 abundances versus the Global Mean Sea Level (GMSL) variations. The central green line shows the linear fit, the red line shows a quadratic fit, wide green lines and wide thin black lines show the 95% confidence level of the data covered by linear and quadratic fits, respectively.

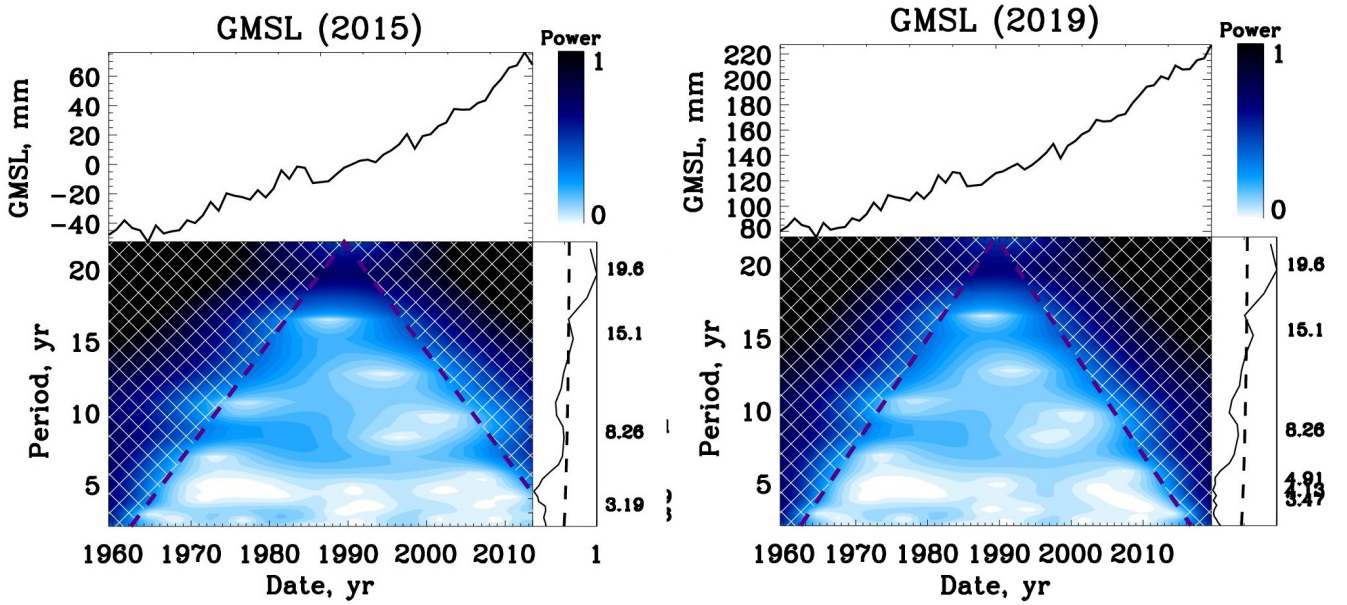

Figure 9. Wavelet spectra of the Global Mean Sea Level (GMSL) taken in 2015 (left image) and in 2019 (right image) datasets (see the text for more details). The GMSL temporal variations are plotted in the top left sides of each image with their wavelet spectra shown in the bottom left sides with the black dashed lines showing the Cone of Influence (COI). The wavelet spectral powers are marked by the colour bars in each image (the top right plots) and the global wavelet spectra (black solid line) integrated over times are shown in the bottom right plots with the black dashed lines indicating the 95% confidence intervals of the detected spectral features.

Let us now apply the Morlet wavelet analysis to the CO_2 abundance and ONI/ENSO sets with the results presented in Fig. 12. The most important feature derived from the ONI/ENSO index is a presence of the statistically significant periods of 3.57-5.05 and 12 years with some tendency to have a double 12 year period restricted by a short length of the ONI/ENSO data (Zharkova & Vasilieva 2024a). The lower period of 4-5 years in the ONI/ENSO index variations can be related to the effects of a half cycle of the lunar perigee oscillation of 8.85 years on the elliptical orbit of the Moon (Zharkova & Vasilieva 2024b) leading to stronger tides twice a year when the lunar perigee is aligned with the Earth-Sun axis leading to the semidiurnal lunar tides (Haigh et al. 2011). This force can lead to the dominant positive Antarctic Oscillation (AAO) (Roy 2018) and increase of volcanic eruptions (Zharkova & Vasilieva 2024b).

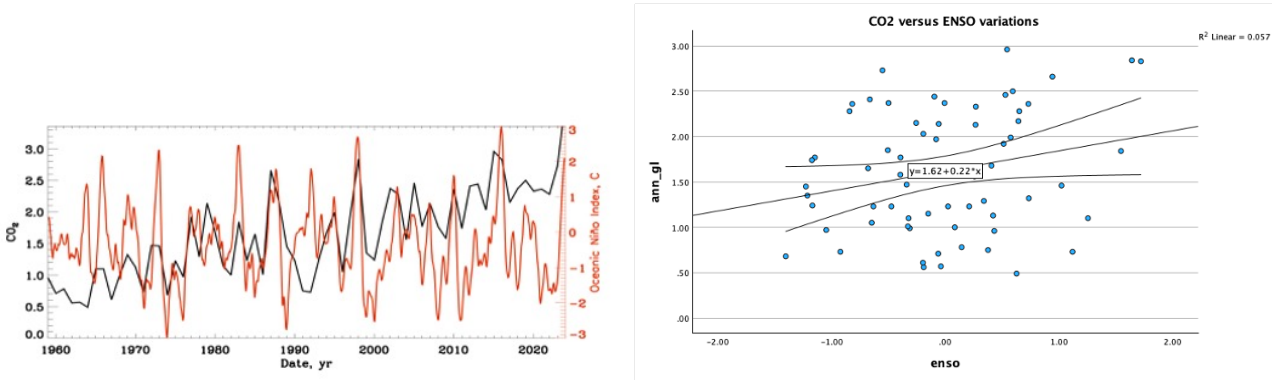

Figure 10. Left plot: the variations of the global CO_2 abundances (black curve) versus the variations of ONI/ENSO (red curve). Right plot: a scatter plot of the correlation (correlation coefficient r=0.24) of the global CO_2 and ONI/ENSO variations.

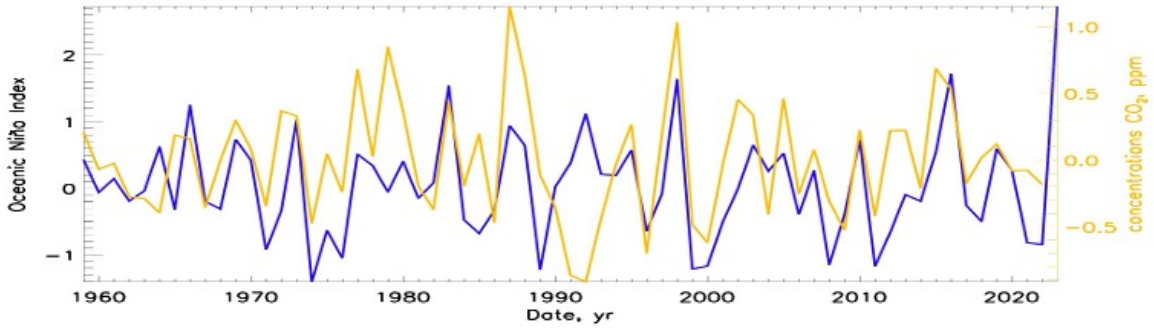

Figure 11. The variations of the de-trended (deviation from average) global CO_2 abundances (yellow curve) versus the ONI/ENSO index variations (purple curve) revealing the correlation coefficient r=0.79.

The larger period of 12 years in the ONI index, which is detected with the high accuracy within 95% confidence interval. This period is not linked to solar activity indices (Zharkova & Vasilieva 2024b), which have the period of 10.7 years (Zharkova et al. 2023a,b). Although, this 12 year period of the ONI/ENSO index oscillations is shown linked to the revolution of Jupiter and its gravitational effects on the Sun in it solar inertial motion Zharkova & Vasilieva (2023).These planetary effects on ONI/ENSO with periods of 4.5-5 and 12 years shown in Fig.12 combined with the correlation of the de-trended CO_2 abundance with ONI/ENSO variations (Fig.11) can help to understand the unusual period of 9 years in CO_2 variations which is likely to indicate the joint effect of the planetary influences of 12 (Jupiter) and 5 (Lunar perigee) years making the difference in the CO_2 abundances to reveal a maximum at the median period of 9 years.

4.2.3. *Variations of CO_2 abundances versus the GLB temperature*

The investigations of the links of CO_2 variations with the sea level and OBI/ENSO index variation brings us to a need to explore the link of CO_2 abundances to the terrestrial temperature variations which are compare directly with the GLB temperature in Fig.13 (left plot) and scatter plot of correlation shown the right plot. It shows a very close (82%) correlation of the CO_2 abundance s with the GLB temperature variation with the linear fit covering most of the data within 95% confidence level. It could be argued that the parabolic fit between the two datasets is aligned better with the data than a linear one. However, this requires more solid verification.

In order to evaluate the spectral properties of the series and to derive the key periods let us apply the Morlet wavelet analysis to the GLB temperature with the results presented in Fig. 14. The most important feature derived from the GLB series of terrestrial temperature is a presence of the statistically significant periods of 21.4 years., similar to the variations of CO_2 and GMSL sea level. The period of 21.4 years is corresponding to the oscillation period of a solar magnetic activity cycle derived in the summary curve of eigen vectors of the SBMF (Zharkova et al. 2023a,b). There is some indication in the GLB temperature variations to a period of 8.26 years that can be related to the period of 9 years found in CO_2 variations.

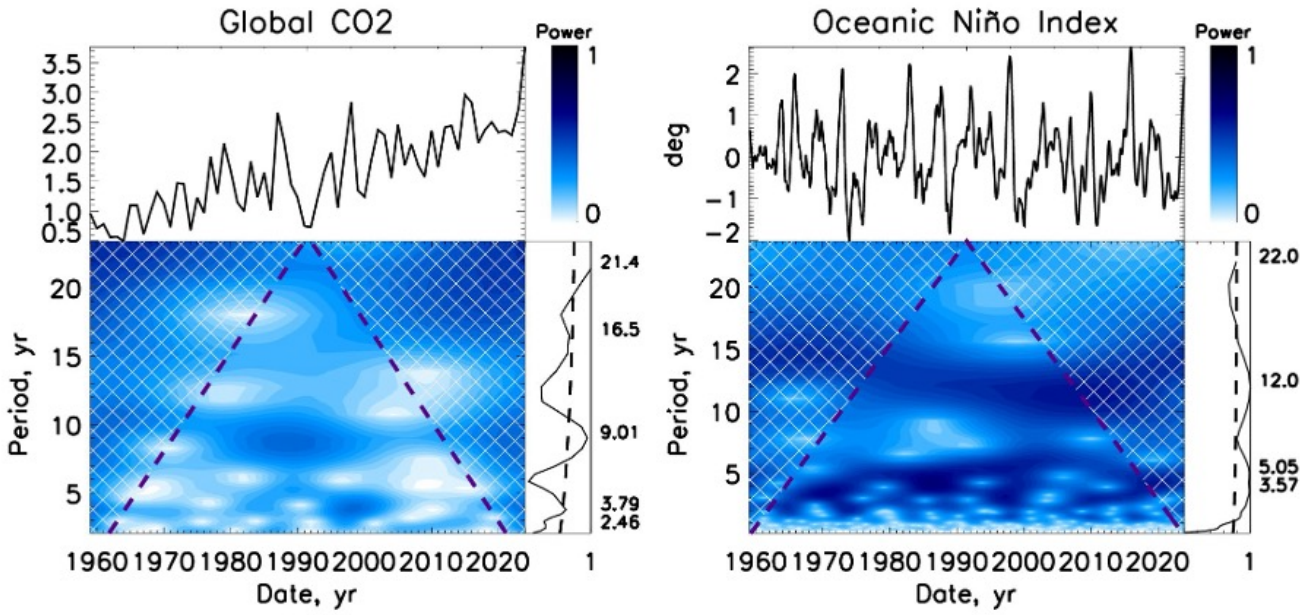

Figure 12. The wavelet analysis of the variations of the global CO_2 abundances (left image) and ONI/ENSO (right image). The CO_2 and ONI/ENSO temporal variations are plotted in the top left sides of each image with their wavelet spectra shown in the bottom left sides of each image. The wavelet spectral powers are marked by the colour bars in each image (the top right plots) and the global wavelet spectra (black solid line) integrated over times are shown in the bottom right plots with the black dashed lines indicating the 95% confidence intervals of the detected spectral features.

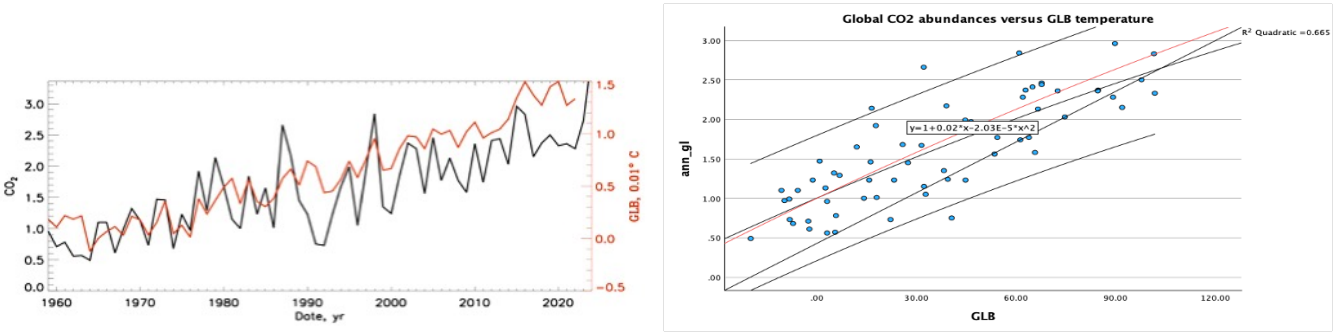

Figure 13. Left plot: the variations of the global CO_2 abundances (black curve) versus the GLB terrestrial temperature (red curve). Right plot: the scatter plot of the correlation (r=0.82) of the global CO_2 abundances versus the global GLB) temperature variations. The red line presents linear fit of CO_2 and temperature, the central thin black line shows quadratic fit. The two thin black lines show the 95% confidence level of the data covered by the fits.

Although this close correlation of two datasets (CO_2 and GLB) does not indicate clearly, which of the datasets is leading and which is lagging. This point can be explored with the cross-correlation and wavelet coherence discussed in the next section.

4.3. *Cross-correlation and wavelet coherences of CO_2 abundances and GLB temperature*

Lets first calculate the traditional cross-correlation of the series of CO_2 abundances and GLB temperatures presented In Fig.15 (top plot). The cross-correlation function clearly reveals the lag by CO_2 abundance of about 1 year from the GLB temperature variations that resembles the similar lag of CO_2 variations reported earlier by Salby & Harde (2022).

To enhance this finding let us now apply the coherence function of the cross-wavelet transform of the series of the CO_2 abundances and the GLB terrestrial temperature with the wavelet coherence spectrum shown in Fig.15 (bottom

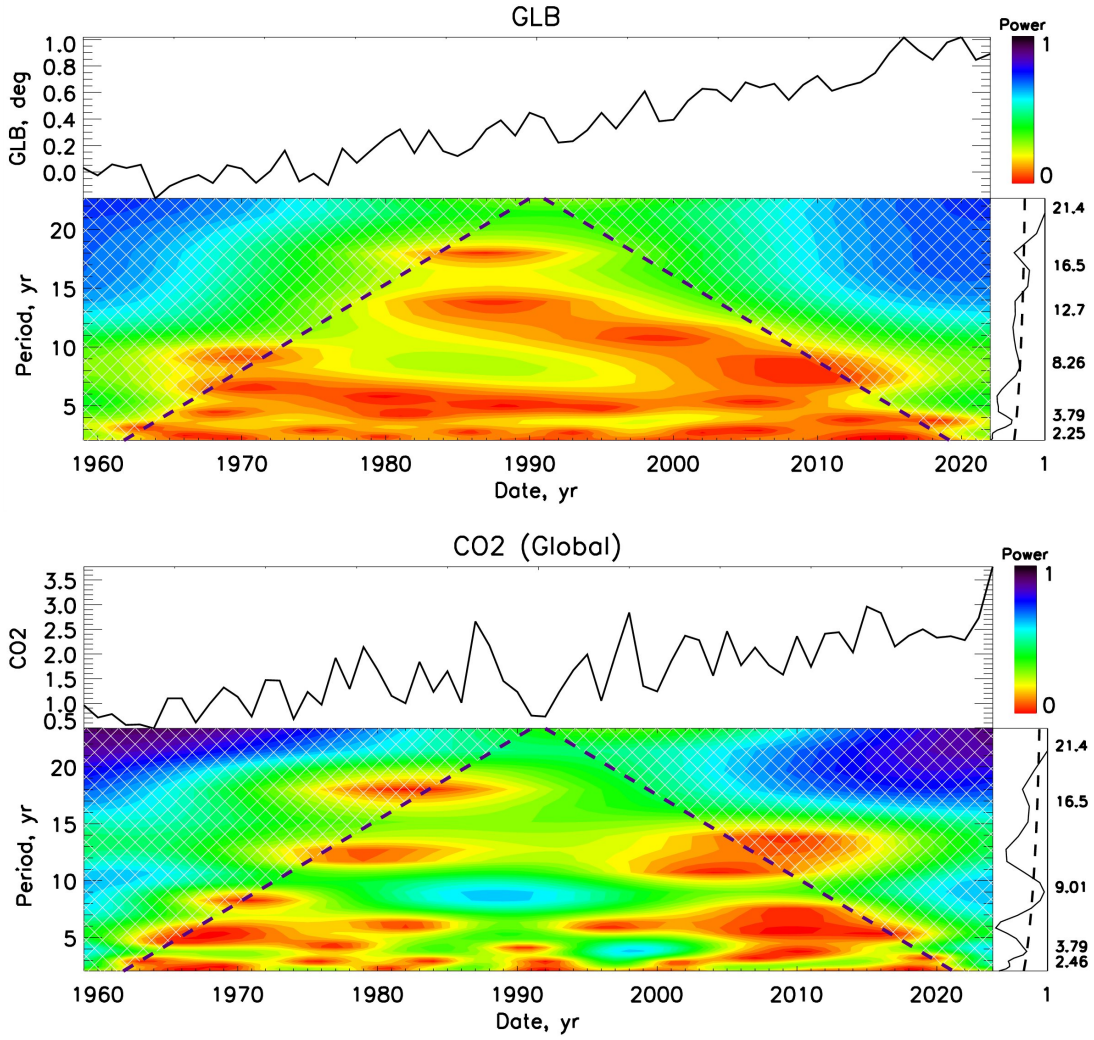

Figure 14. The wavelet analysis of the variations of the global GLB temperature (top image) and the global CO_2 abundances (bottom image). The GLB temperature and CO_2 variations are plotted in the top left sides of each image with their wavelet spectra shown in the bottom left sides of each image. The wavelet spectral powers are marked by the colour bars in each image (the top right plots) and the global wavelet spectra (black solid line) integrated over times are shown in the bottom right plots with the black dashed lines indicating the 95% confidence intervals of the detected spectral features.

plot). The darker parts of the wavelet coherence spectrum correspond to a higher correlation (90% or higher) of the CO_2 and GLB temperature series while the lighter parts denote a weak correlation. The arrows indicate the phase shifts between the two series under the investigation for the intervals where the cross-correlation is higher than 0.9.

The arrow inclination to right (or left) indicates the series to be in phase (or anti-phase). A zero difference would indicate the series move coherently, the arrow inclination towards right indicate that the series of the CO_2 abundance lags the GLB temperature series. Hence, the arrows on the wavelet coherence plot indicate the phase relationship between the series, either moving forward or lagging. The angle of arrow inclination indicates the phase shift $\Delta\phi$ which can be linked to the time lag Δ_t as described in section 3.2.

We use the phase angle shift $\Delta\phi$ (Eq.5) obtained on the 8 years scale for the strongest correlation of 0.9 shown in Fig.15 (bottom plot) for the two series of CO_2 and GLB temperature variations and convert it into the time lag Δ_t using formula (Eq.6). The positive Δt indicates there is a time lag (delay) of the CO_2 abundance variations with respect to the terrestrial GLB temperature series.

This coherence wavelet analysis revealing the strongest correlation (r>0.9) of these two datasets allowed us to obtain a time difference for variations of CO_2 abundances and the GLB temperature to be equal to 1.2-1.8 years in the periods

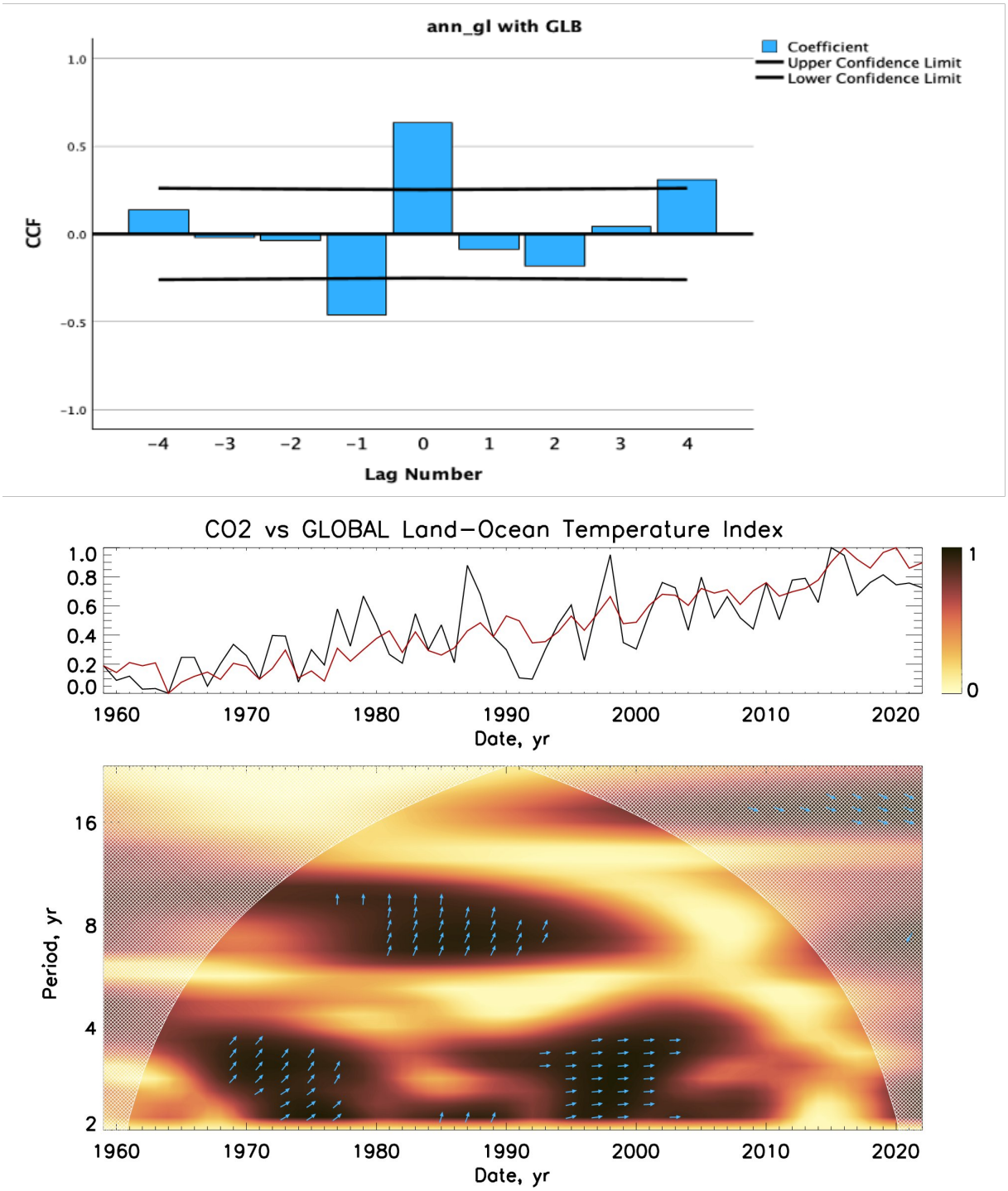

Figure 15. Top plot: cross-correlation of the global CO_2 variation and GLB temperature showing the time lag of CO_2 at least one year from GLB temperature. Bottom plot: the wavelet cross-correlation and coherence function showing a lag of CO_2 abundances from the GLB temperature by 1.2-1.8 years (see details in the text).

of >4 (1970- 1975) or > 8 (1980-1990) years. There was a coherence between these two datasets in 1995-2005 when the arrows become parallel to the X-axis as derived with wavelet coherence analysis in Fig.15 (bottom plot). This indicates the two datasets, CO_2 and temperature can occasionally appear coherently with a period of 4 years while CO_2 abundances definitely lag the temperature variations with a period of 8 years.

This lag size of 1.2-1.8 years between the variations of CO_2 abundance and terrestrial temperature for a period of 8 years confirms more accurately the time lag of one year detected for the whole datasets using the cross-correlation function shown in Fig.15 (top plot). This indicates that the CO_2 abundances follows the variations of terrestrial GLB temperature and not define them. Hence, carbon dioxide cannot be the force, which induces the temperature variations. The most likely force imposing the terrestrial temperature variation was suggested to have the links to solar radiation emitted either owing to solar magnetic activity with a period of 21.4 years or modulated by the orbital motion of the Sun and planets via their links with ONI/ENSO index.

5. DISCUSSION AND CONCLUSIONS

In this study we investigate the measurements of the total CO_2 abundances recorded at the US Samoa and Mauna Loa observatories as well as the global CO_2 variations produced from all the sets CO_2 observations at NOAA. The global CO_2 abundance variations were compared directly with variations of the global mean sea level (GMSL), ONI/ENSO variations and the global (GLB) terrestrial temperature. Annual variations of the CO_2 abundances are shown to have the best fit by a parabolic curve with concavity up while the linear fit has shown systematic deviations indicating the CO_2 curve parabolic curvature. Hence, the measurements of the total (global) annually averaged CO_2 variations, which by default should be present in the measured data, do not reveal any noticeable similarity to the linear CO_2 abundances produced by the fossil fuel usage.

Although, there is a good correlation (r=0.60) between CO_2 abundances variations and the seal level GMSL datasets and much stronger correlation (0.82) of CO_2 variations and the GLB terrestrial temperature. The link of CO_2 variations to the ONI/ENSO index is not very strongly correlated (r=0.24), while the with the ONI/ENSO index is shown to have stronger correlation (r=0.79) with the de-trended variations of CO_2 above the averaged level is highly that indicates to a complex effect of the CO_2 exchange between sea and air governed by ONI/ENSO.

Spectral analysis with Morlet wavelet transform reveal the wavelet spectra of global and MLO CO_2 variations to have well-defined (above 95% confidence level) periods of oscillation of 21.4 and 9 years and the period of 3.79 years occurring within the 95% confidence level. Moreover, the wavelet analysis allowed to uncover the key periods of the variations of CO_2 (21.4, 9 and 3.7 years), GMSL (21.4, 8.5 years), ENSO (21.4, 12 and 4.5 years) and terrestrial temperature (21.4, 8.36 and 3.75 years).

The presence of a common period of 21.4 years in all the datasets including CO_2 abundances indicates that these datasets are affected by the same natural source, namely, by the cyclic variations of solar background magnetic field in double cycle of solar activity (Zharkova et al. 2015). The CO_2 abundance oscillations with a period of 9 years can be linked by the variations ONI/ENSO with periods of 4.5and 12 years which combined with the correlation of the de-trended CO_2 abundance with ONI/ENSO variations can explain how ONI/ENSO index can induce the observed CO_2 variations. This period is likely to indicate the joint effect of the planetary influences on the ONI/ENSO index of 12 year (Jupiter) and 4.5-5 years (Lunar perigee) which make the maximum difference in the CO_2 abundances at the median period of 9 years. Thus, the natural periods of CO_2 abundance oscillations linked to the similar periods in GMSL and ONI/ENSO indices indicates that the production of CO2 on Earth is governed by natural processes of the air-ocean exchanges modulated by the variations of solar magnetic field.

The most important correlation (r=0.89) is found between the variations of the global CO_2 abundances and GLB terrestrial temperature indicating a strong relationship between these two entities. The cross-correlation analysis allowed us to establish the time lag of one year for the CO_2 abundance from the GLB temperature variations, which was preciously reported by other researchers (Salby & Harde 2022). Furthermore, the coherence wavelet analysis of the global CO_2 and GLB terrestrial temperature variations established their strong correlation (r¿0.9) and derived that CO_2 abundance variations lags lags the temperature variations by 1.2-18 years during the most intervals of observations.

From the present analysis it becomes more clear that the main variations of the carbon dioxide abundances mainly have natural causes linked to the solar activity, exchange of CO_2 between the air and ocean and some other planetary effects via ONI/ENSO variations. If there are any additions to the current CO_2 abundances by the anthropogenic use of the carbon dioxide in fossil fuel, these additions must be much smaller than the natural effects on the terrestrial environment imposed by the solar magnetic field, gravitation of the Sun, planets and moon, which define the key periods of the carbon dioxide variations.

6. ACKNOWLEDGMENTS

The authors wish to express their many thanks for the data provided by the NOAA's Global Monitoring Laboratory (GML), which measures the abundances of carbon dioxide and other greenhouse gasses. We also appreciate the NASA Goddard Institute of Space Science (GISS) (US) and the British meteorological Center in Hadley, for providing the temperature datasets, the Centre for protection of the environment of the USA and the Centre for Scientific and Industrial Research Organisation for providing the data of the sea level and ONI/ENSO.

7. OPEN RESEARCH

The freely available datasets used in this study are listed below.

1. NOAA's General Monitoring Laboratory (GML) CO2 datasets (Thoning et al. 1989; Conway et al. 1994; Lan et al. 2026). This dataset was produced by NOAA and is not subject to copyright protection in the United States. NOAA waives any potential copyright and related rights in these data worldwide through the Creative Commons Zero v1.0 Universal Public Domain Dedication (CC0 1.0) (Lan et al. 2026).

   (a) Globally averaged marine surface CO_2 annual mean data (Lan et al. 2026): https://gml.noaa.gov/ccgg/trends/gl_data.html; https://gml.noaa.gov/webdata/ccgg/trends/co2/co2_annmean_gl.txt.

   (b) Globally averaged marine surface annual mean CO_2 growth rates (Lan et al. 2026): https://gml.noaa.gov/ccgg/trends/data.html; https://gml.noaa.gov/webdata/ccgg/trends/co2/co2_gr_gl.txt.

   Other NOAA GML CO_2 datasets (Lan et al. 2026):

   (a) Mauna Loa CO_2 annual mean growth rates (Keeling et al. 1976; Thoning et al. 1989): https://gml.noaa.gov/webdata/ccgg/trends/co2/co2_gr_mlo.txt.

   (b) Mauna Loa CO_2 annual mean data (Keeling et al. 1976; Thoning et al. 1989): https://gml.noaa.gov/webdata/ccgg/trends/co2/co2_annmean_mlo.txt.

   (c) Samoa Observatory data (Lan et al. 2026): https://gml.noaa.gov/data/dataset.php?item=smo-co2-flask-month
   This dataset was produced by NOAA and is not subject to copyright protection in the United States. NOAA waives any potential copyright and related rights in these data worldwide through the Creative Commons Zero v1.0 Universal Public Domain Dedication (CC0 1.0) (Lan et al. 2026).

2. The Global Mean Sea Level (GMSL) datasets:

   (a) GMSL dataset obtained during 1880-2014 (named GMSL(2015)) was obtained from the Centre for Protection of the Environment of the USA and SCIRO (Centre for Scientific and Industrial Research Organisation) http://data-cbr.csiro.au/thredds/catalog/catch_all/OA_SLE_processed/Sea_Level_data/gmsl_files/catalog.html accessed on 29/07/2023 (Church & White 2011).

   (b) The same GMSL dataset extended to 2019 (named GMSL(2019)) was accessed on 25/05/2025, http://data-cbr.csiro.au/thredds/catalog/catch_all/OA_SLE_processed/Sea_Level_data/gmsl_files/catalog.html.

3. Terrestrial temperature datasets:

   (a) HadCRUT5 - the British Meteorological Center in Hadley and the department of Climate Research of the East Anglia University https://www.metoffice.gov.uk/hadobs/hadcrut5/, accessed on 12/06/2023 (Morice et al. 2021).

   (b) GLB: the surface temperature (GISSTEMP) produced by the NASA Goddard Institute of Space Science (GISS) https://data.giss.nasa.gov/gistemp/tabledata_v4/GLB.Ts+dSST.txt accessed 12/06/2023; https://data.giss.nasa.gov/gistemp/tabledata_v4/GLB.Ts+dSST.txt (Lenssen et al. 2019).

4. The Oceanic Niño Index (ONI) which also called as El Nina Southern Oscillation (ENSO), e.g. the Niño 3.4 index available since 1854 is taken from https://www.climate.gov/news-features/understanding-climate/climate-variability-oceanic-nino-index (Kaplan et al. 1998).

Software used for analysis:

1. Wavelet analysis software in IDL was provided by Torrence & Compo (1998), available at http://paos.colorado.edu/research/wavelets/.

2. IBM SPSS Statistics v30.0 https://www.ibm.com/products/spss-statistics/gradpack is a comprehensive statistical analysis platform designed to help organisations and individuals extract reliable insights from data. It combines robust statistical testing, predictive modelling, regression, and forecasting with streamlined data preparation and automated analysis. With integrated AI capabilities, including the AI Output Assistant, users can interact with results using natural language - making complex outputs easier to understand and act on.

   Authorised user licence is required and updated every year https://www.ibm.com/products/spss-statistics?utm_content=SRCWW&p1=Search&p4=299294893835&p5=e&p9=171934014643&gclsrc=aw.ds&gad_source=1&gad_campaignid=22037412442&gbraid=0AAAAA-h2TOF3_WUtiv6WG-ci1rXhdeU3X&gclid=EAIaIQobChMIu5vOkOCilAMVe5JQBh1XhikpEAAYASAAEgKWrfD_BwE.

AUTHOR CONTRIBUTIONS STATEMENT

V.Z. formulated the problem, suggested the datasets to consider, did calculations and statistical analysis of the datasets with SPSS provided by IBM. I.V. gathered and processed the temperature, sea level data and ONI/ENSO index, analysed them with the wavelet tool, plotted the graphs. V.Z. and I.V. compared and analysed the results, wrote and reviewed the manuscript.

ADDITIONAL INFORMATION

The authors do not have any competing financial interests.

REFERENCES

Ahlbeck, J. R. 2009, Energy and Environment, 20, 1149, doi: 10.1260/095830509789876772

Ato, D. 2024, Science of Climate Change, 4.2, 1, doi: 10.53234/SCC202407/19

Cazenave, A., & Nerem, R. 2004, Rev. Geophys, 42, doi: 10.1029/2003RG000139

Church, J., & White, N. 2011, Surveys in Geophysics, 32, 585, doi: 10.1007/s10712-011-9119-1

Church, J. A., & White, N. J. 2006, Geophysical Research Letters, 33, L01602, doi: 10.1029/2005GL024826

Conway, T. J., Tans, P. P., Waterman, L. S., et al. 1994, Journal of Geophysical Research: Atmospheres, 99, 22831, doi: https://doi.org/10.1029/94JD01951

Easterbrook, D. J. 2016, Evidence-based Climate Science (Elsevier)

Fox-Kemper, B., Hewitt, H., Xiao, C., et al. 2021, Ocean, Cryosphere and Sea Level Chang (Cambridge, United Kingdom and New York, NY, USA: Cambridge University Press), 1211–1362, doi: 10.1017/9781009157896.011

Gervais, F. 2016, Earth Science Reviews, 155, 129, doi: 10.1016/j.earscirev.2016.02.005

Grinsted, A., Moore, J. C., & Jevrejeva, S. 2004, Nonlinear Processes in Geophysics, 11, 561, doi: 10.5194/npg-11-561-2004

—. 2010, Climate Dynamics, 34, 461, doi: 10.1007/s00382-008-0507-2

Haigh, I. D., Eliot, M., & Pattiaratchi, C. 2011, Journal of Geophysical Research (Oceans), 116, C06025, doi: 10.1029/2010JC006645

Henry, W. 1803, Philosophical Transactions of the Royal Society of London Series I, 93, 29

Humlum, O., Stordahl, K., & Solheim, J.-E. 2013, Global and Planetary Change, 100, 51, doi: 10.1016/j.gloplacha.2012.08.008

IPCC. 2025, The Physical Science Basis, doi: 10.1029/2004GL019626

Jaworowski, Z., Segalstad, T. V., & Ono, N. 1992, Science of the Total Environment, 114, 227, doi: 10.1016/0048-9697(92)90428-U

Kaplan, A., Cane, M. A., Kushnir, Y., et al. 1998, Journal of Geophysical Research: Oceans, 103, 18567, doi: 10.1029/97JC01736

Keeling, C. D., Bacastow, R. B., Bainbridge, A. E., et al. 1976, Tellus, 28, 538, doi: 10.1111/j.2153-3490.1976.tb00701.x

Koutsoyiannis, D., Onof, C., Kundzewicz, Z., & Christofides, A. 2023, MDPI Sci, 5, 35, doi: 10.3390/sci5030035

Lan, X., Tan, P., & Thoning, K. W. 2026, MDT Tuesday 5 May 2026), doi: 10.15138/9N0H-ZH07

Lenssen, N. J. L., Schmidt, G. A., Hansen, J. E., et al. 2019, Journal of Geophysical Research: Atmospheres, 124, 6307, doi: https://doi.org/10.1029/2018JD029522

Leuliette, E. W., Nerem, R. S., & Mitchum, G. T. 2004, Marine Geodesy, 27, 79

Morice, C. P., Kennedy, J. J., Rayner, N. A., et al. 2021, Journal of Geophysical Research (Atmospheres), 126, e2019JD032361, doi: 10.1029/2019JD032361

Nerem, R. S., Beckley, B. D., Fasullo, J. T., et al. 2018, Proceedings of the National Academy of Science, 115, 2022, doi: 10.1073/pnas.1717312115

Rahmstorf, S. 2007, Science, 315, 368, doi: 10.1126/science.1135456

Roy, I. 2018, Frontiers in Earth Science, 6, 136, doi: 10.3389/feart.2018.00136

Salby, M., & Harde, H. 2022, Science of Climate Change, 2.3, 212, doi: 10.53234/scc202212/17

Salby, M. L., Titova, E. A., & Deschamps, L. 2012, Journal of Geophysical Research (Atmospheres), 117, D10111, doi: 10.1029/2011JD016285

Sannino, G., Carillo, A., Iacono, R., et al. 2022, Climate Dynamics, 59, 357, doi: 10.1007/s00382-021-06132-w

Soares, P. C. 2010, International Journal of Geosciences, 1, 102, doi: 10.4236/ijg.2010.13014

Storch, H. V., Zorita, E., & González-Rouco, J. F. 2008, Ocean Dynamics, 58, 227, doi: 10.1007/s10236-008-0142-9

Thoning, K. W., Tans, P. P., & Kornhyr, W. D. 1989, Journal of Geophysical Research: Atmospheres, 94, 8549

Torrence , C., & Compo, G. P. 1998, Bull. of American Meteorological Society, 79, 61, doi: https://psl.noaa.gov/people/gilbert.p.compo/Torrence_compo1998.pdf

Trenberth, K. E., & Fasullo, J. T. 2009, Geophysics Research Letters, 36, L07706, doi: 10.1029/2009GL037527

Vasilieva, I., & Zharkova, V. 2023, Global Journal of Science Frontier Research, 23, 22pp, doi: 2249-4626

Vermeer, M., & Rahmstorf, S. 2009, Proceedings of the National Academy of Science, 106, 21527, doi: 10.1073/pnas.0907765106

Veyres, C., Maurin, J.-C., & Poyet, P. 2024, Science of Climate Change, 5, 155, doi: 10.53234/scc202510/10

Zharkova, V. V., Shepherd, S. J., Popova, E., & Zharkov, S. I. 2015, Scientific Reports, 5, 15689, doi: doi:10.1038/srep15689

Zharkova, V. V., & Vasilieva. 2023, Natural Science, 15, 233, doi: 10.4236/ns.2023.159018

—. 2024a, Natural Science, 16, 25, doi: 10.4236/ns.2024.164004

—. 2024b, Atmospheric and Climate Sciences,, 15, 25, doi: 10.4236/acs.2025.151004

Zharkova, V. V., Vasilieva, I., Popova, E., & Shepherd, S. J. 2023a, *Monthly Notices Royal Astron. Soc.*, 521, 6247, doi: 10.1093/mnras/stad1001

Zharkova, V. V., Vasilieva, I., Shepherd, S., & Popova, E. 2023b, Natural Science, 15, 56 pp, doi: 10.4236/ns.2023.153010